The $3\,^2S_{1/2}$-$3\,^2D_{5/2}$ interval in atomic hydrogen. III. Separated-oscillatory-field measurement

D. A. Van Baak,* B. O. Clark,† S. R. Lundeen, and F. M. Pipkin
Lyman Laboratory of Physics, Harvard University, Cambridge, Massachusetts 02138
(Received 9 October 1979)

This paper reports the use of oscillatory fields in two spatially separated interaction regions to make a two-quantum radio-frequency measurement of the $3\,^2S_{1/2}$-$3\,^2D_{5/2}$ fine-structure interval in atomic hydrogen. The measurement was carried out in zero magnetic field with a fast hydrogen beam. Radio-frequency fields from two separate oscillators were applied in both interaction regions and used to drive the two-quantum transition. The relative phase in the two interaction regions of one of the radio-frequency fields was alternated between 0° and 180° so as to isolate the separated-oscillatory-field interference signal; the frequency of the other radio-frequency field was varied so as to sweep over the resonance. An adaptation of the earlier reported theory was used to calculate the line shape and power dependence of the separated-oscillatory-field interference signal. The measured value for the $3\,^2S_{1/2}$-$3\,^2D_{5/2}$ interval is 4013.106(57) MHz. This value agrees satisfactorily with both the previously reported single-radio-frequency-field measurement and the theoretical value for this interval. The value for the $3\,^2S_{1/2}$-$3\,^2D_{5/2}$ interval obtained by combining the results from this measurement with the single-field measurements reported earlier is 4013.155(53) MHz.

I. INTRODUCTION

In two earlier papers[1,2] we reported a theoretical calculation of the line shape for the two-phonon $3\,^2S_{1/2}$-$3\,^2D_{5/2}$ transition in atomic hydrogen and a measurement of this fine-structure interval. These papers dealt only with the situation in which a fast atomic beam passes through a single interaction region in which a radio-frequency field is present. In this paper we report a measurement in which two spatially separated oscillatory-field regions were used to measure the $3\,^2S_{1/2}$-$3\,^2D_{5/2}$ fine-structure interval. The theoretical methods developed earlier are used to calculate the line shape and power shift for the configuration with two radio-frequency fields.

In the measurements with a single oscillatory field, the linewidth is limited by both the transit time and the natural linewidth. In the earlier measurements the linewidth was roughly 25 MHz compared to the fine-structure interval of 4040 MHz, and the 10-MHz natural linewidth due to the lifetime of the states. In the separated-oscillatory-field measurement reported here we were able to obtain linewidths of 6 to 8 MHz.

The combination of Ramsey's method of separated oscillatory fields and fast-beam spectroscopy has been used by Fabjan and Pipkin to measure the Lamb shift in the $n=3$ state of hydrogen[3] and by Lundeen and Pipkin to measure the Lamb shift in the $n=2$ state of hydrogen.[4] The first-fast-beam observation of the $3\,^2S_{1/2}$-$3\,^2D_{5/2}$ two-photon transition was reported by Kramer *et al.*,[5] who also used two separated oscillatory fields to observe the interference pattern by switching the relative phase of the two fields between 0° and 90°.

The measurement reported here uses two radio-frequency fields oscillating at angular frequencies ω_1 and ω_2 in each of the two separated-field regions. Frequency component ω_1 is applied with 0° phase difference in each of the two interaction regions and is scanned to trace out the two-photon resonance. Frequency component ω_2 is kept fixed in frequency, but is applied to the two interaction regions with 0° or 180° relative phase. The difference between the signals obtained with 0° and 180° relative phase shows an interference signal centered at $\omega_1+\omega_2=\omega(^2S_{1/2}$-$^2D_{5/2})$, corresponding to a two-photon transition involving one ω_1 and one ω_2 photon. This technique avoids the difficult problem of generating a 90° phase shift which is independent of frequency. This technique was first demonstrated by Clark *et al.*[6] for the hydrogen $3\,^2S_{1/2}$-$3\,^2D_{5/2}$ transition.

This paper reports in succession the description of the technique, the theory for the two-photon–two-frequency line shape, the apparatus, the data-taking procedure, the results, and the conclusions.

II. DESCRIPTION OF THE TECHNIQUE

In undertaking this measurement, we were strongly motivated by two observations. First, multiple-quantum measurements provide high-Q resonances which can be used to determine the fine structure of hydrogenlike atoms. The conventional methods for measuring the fine structure of hydrogenic atoms use radio-frequency transitions between the long-lived $n\,^2S_{1/2}$ states and the shorter-lived $n\,^2P_{1/2,3/2}$ states. The ultimate accuracy of the measurements is limited by the linewidth, which is determined primarily by the short lifetimes of the $n\,^2P_{1/2,3/2}$ states. The $3\,^2S_{1/2}$-$3\,^2D_{5/2}$ double-quantum transition has one-third the natural linewidth of the $3\,^2S_{1/2}$-$3\,^2P_{1/2,3/2}$ transitions

because the lifetime of the $3^2D_{5/2}$ state is three times that of the $3^2P_{3/2}$ state. The increase in Q is even more spectacular if one considers multiple-quantum transitions in high-n manifolds from the $n^2S_{1/2}$ state to the highest angular-momentum state in that manifold. This improved linewidth is partly offset by the large power shifts encountered with multiple-quantum transitions.

The second observation is that the combination of a fast atomic beam and two separated-oscillatory-field regions makes it possible to work with short-lived states and to reduce significantly the power shift. The feasibility of working with short-lived states makes it feasible to carry out experiments on the higher excited states of helium where the increase in Q is particularly attractive. The existence of a field-free region between the two separated oscillatory fields reduces the rf Stark shift and makes the power correction less serious.

Since the multiple-quantum measurements are an extension of the single-quantum separated-oscillatory-field measurements, it is instructive to review briefly the single-quantum separated-oscillatory-field technique. In the single-quantum separated-oscillatory-field experiments, a fast beam of hydrogen atoms in the $n^2S_{1/2}$ state with a well-defined velocity is produced by charge-exchange collisions between an incident proton beam and a gaseous target. The beam of atoms then passes sequentially through rf field A, a field-free region, and rf field B. The number of atoms that emerge from B in the $n^2S_{1/2}$ state is monitored so that the relevant quantity is the transmission probability for atoms in the $n^2S_{1/2}$ state to pass through the two rf fields. There are two "paths" through which atoms initially in the $n^2S_{1/2}$ state can be transmitted through the spectroscopy region. One path (the S path) is via the $n^2S_{1/2}$ state in the field-free region; the other path (the P path) is via the $n^2P_{1/2}$ state in the field-free region. When summed and squared, the amplitudes for these two paths give the total transmission probability. The various contributions to the amplitudes are illustrated by the diagrams in Fig. 1.

The amplitudes can be calculated using time-dependent perturbation theory, and it is convenient to use the language of time-depepdent perturbation theory to describe the transitions. For each absorption (emission) of an rf photon, the corresponding amplitude acquires a phase factor of $e^{-i\theta}$ ($e^{+i\theta}$) and a multiplication factor E, where θ is the phase of the rf electric field and E is the strength of the rf electric field. If θ_A denotes the phase in field region A and θ_B that in B, the S path has a net phase factor of unity, and the P path has a net phase factor of $\exp[i(\theta_A - \theta_B)]$. In summing and squaring the S and P amplitudes, a cross

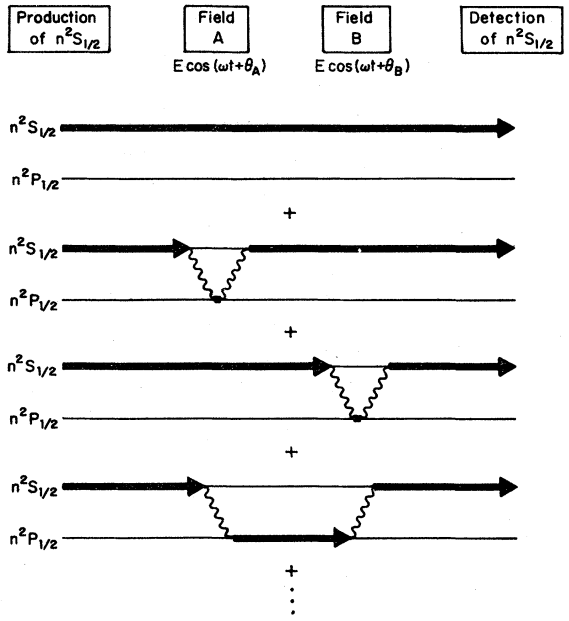

FIG. 1. A schematic representation of contributions to the amplitude for a hydrogen atom to enter and emerge from the separated-oscillatory-field interaction region in an $n^2S_{1/2}$ state when there is present an rf field of sufficient strength and with the required frequency to drive the $n^2S_{1/2}-n^2P_{1/2}$ single-photon transition.

term emerges with a phase of $(\theta_A - \theta_B)$. This cross term can be isolated from the total signal if data taken with $(\theta_A - \theta_B)$ set at 180° are subtracted from data taken with $(\theta_A - \theta_B)$ set at 0°. The squares of the P-path amplitude and the S-path amplitude do not contain this phase factor and thus cancel in the subtraction. The interference term describes atoms which pass without radiative decay through the entire spectroscopy region. Thus the linewidth for the interference term is determined by the transit time between the two rf fields, and not by the lifetimes of the states.

The signal obtained by averaging the data taken with $(\theta_A - \theta_B)$ set at 180° and the data taken with $(\theta_A - \theta_B)$ set at 0° is called the quenching signal. It is the separated-oscillatory-field analog of the single-oscillatory-field signal.

The simplest scheme for extending the separated-oscillatory-field method to the two-quantum $3^2S_{1/2}$-$3^2D_{5/2}$ transition is to use the same procedure as with the single-quantum transition but with a different choice for $\theta_A - \theta_B$. In this case, an atom entering field-region A in the $3^2S_{1/2}$ state can make a transition to the $3^2D_{5/2}$ state through the absorption of two photons if $2\hbar\omega \simeq [E(^2D_{5/2}) - E(^2S_{1/2})]$. Since the $3^2P_{1/2,3/2}$ states are far from resonance, transitions to these states can be neglected. Thus, there are two paths through which atoms entering region A in the $3^2S_{1/2}$ state

may exit region B in the $3^2S_{1/2}$ state. They are the "S" and "D" paths depicted graphically in Fig. 2. For path D, absorption of two rf photons in region A is followed by emission of two rf photons in region B. As a result the amplitude for the D path has a net phase factor $\exp[2i(\theta_B - \theta_A)]$. The net phase factor for the S path is one. Hence the cross term arising from the square of the sum of the amplitudes has a phase of $2(\theta_B - \theta_A)$; the interference effect can be isolated by subtracting data taken with $(\theta_B - \theta_A)$ equal to 90° from data with $(\theta_B - \theta_A)$ equal to 0°.

From an experimental viewpoint, however, this procedure is unsatisfactory for a precision measurement because it is difficult to produce accurately a relative phase of 90°. A critical component to the success of the separated-oscillatory-field measurement of the Lamb shift in the $n=2$ state of hydrogen is the use of a precision "magic tee" to obtain relative phases of 0° and 180°. The operation of magic tees depends upon symmetry considerations which are not readily applicable to 0° and 90° phase division. In order to overcome this difficulty we developed a two-frequency technique which makes use of a magic tee to obtain the required phase division. The two frequencies, ω_1 and ω_2, which are present in both interaction regions, are chosen so that $\hbar(\omega_1+\omega_2) \simeq [E(^2D_{5/2}) - E(^2S_{1/2})]$ but such that neither frequency is resonant with any single-quantum transition in the $n=3$ manifold. An atom entering field A in the $3^2S_{1/2}$ state can undergo a transition to the $3^2D_{5/2}$ state by absorbing one photon of frequency ω_1 and one photon of frequency ω_2. Similarly, transitions back to the $3^2S_{1/2}$ state can occur in region B if one photon of each frequency is emitted. If we denote the phases of the two-frequency components in region A as θ_{1A} and θ_{2A}, and in region B as θ_{1B} and θ_{2B}, the net phase factor for the D path is

$$\exp\{i[\theta_{1B} - \theta_{1A}) + (\theta_{2B} - \theta_{2A})]\}. \quad (1)$$

By always keeping $(\theta_{1B} - \theta_{1A})$ set at 0°, the interference cross term has the phase of $(\theta_{2B} - \theta_{2A})$. The interference signal can now be isolated from the total signal by subtracting data taken with $(\theta_{2B} - \theta_{2A})$ set at 180° from data taken with $(\theta_{2B} - \theta_{2A})$ set at 0°.

The use of two rf frequencies not only allows the use of a magic tee, but also yields an additional advantage. By always keeping ω_2 fixed in frequency while scanning ω_1 to trace out the resonance line shape, the apparatus becomes insensitive to spurious signals traceable to higher-n states. In a fast-atomic-beam experiment high-n states are usually heavily populated by the charge-exchange process. In an experiment such as this, where the survival of $3^2S_{1/2}$ states is monitored by observing Balmer-alpha photons, only 5% of the optical photons detected originate from atoms which enter the spectroscopy region in the $3^2S_{1/2}$ state. Transitions induced by the spectroscopy fields in high-n levels can be detected by cascade into Balmer-alpha light, and can distort the desired resonance. Since ω_2 is fixed in frequency, transitions induced by this frequency can only produce a constant signal, which vanishes upon subtracting 180° data from 0° data. Transitions in higher-n levels driven by the field of frequency ω_1 also vanish in the subtraction of data since the phase $(\theta_{1B} - \theta_{1A})$ is kept fixed. Only multiple-quantum transitions which involve both ω_1 and ω_2 photons remain after subtraction of data, and in hydrogen there are no such multiple-quantum transitions overlapping the $3^2S_{1/2} - 3^2D_{5/2}$ resonance.

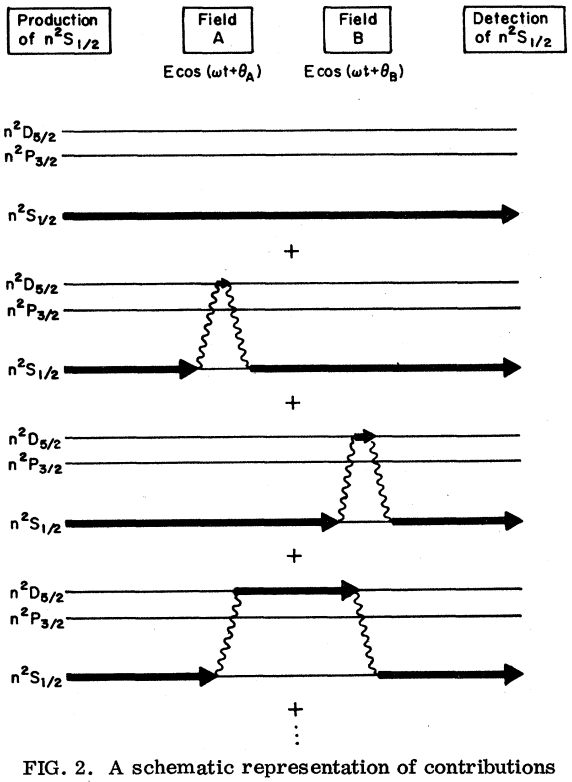

FIG. 2. A schematic representation of contributions to the amplitude for a hydrogen atom to enter and emerge from the separated-oscillatory-field interaction region in a $3^2S_{1/2}$ state when there is present an rf field of sufficient strength and with the required frequency to drive the $3^2S_{1/2} - 3^2D_{5/2}$ two-photon transition.

III. THEORETICAL TREATMENT OF THE LINE SHAPE

In this section we will use the technique reported earlier to calculate the line shape and power shift for the two-quantum, two-frequency signal ob-

served in this experiment. The goal of the calculation is a detailed theory of the transmission of hydrogen atoms in the $3\,^2S_{1/2}(F=0)$ state through the spectroscopy region. For this calculation we will use units in which $\hbar=1$, but leave $\hbar$ in place on occasion for mnemonic reasons. We will take as the $\hat{z}$ axis the direction of polarization of the rf electric field and use this direction as the axis of quantization.

Figure 3 shows a schematic view of the spectroscopy region. In making the calculation we will take as the zero of time, the time at which the atom enters the first waveguide. To a good approximation each atom sees an electric field given by

$$\vec{E}(t)=\begin{cases}\hat{z}E_{1A}\sin(\pi t/\tau)\cos(\omega_1 t+\delta_1) & \\ \quad +\hat{z}E_{2A}\sin(\pi t/\tau)\cos(\omega_2 t+\delta_2), & 0<t<\tau \quad (2)\\ \hat{z}E_{1B}\sin[\pi(t-T-\tau)/\tau]\cos(\omega_1 t+\delta_1+\psi_1) & \\ \quad +\hat{z}E_{2B}\sin[\pi(t-T-\tau)/\tau]\cos(\omega_2 t+\delta_2+\psi_2), & \\ & \tau+T<t<2\tau+T \quad (3)\end{cases}$$

$E(t)=0$ elsewhere. Here τ is the time spent in the first and second waveguides, and T is the time spent in the field-free region between the two waveguides. The phases δ_1 and δ_2 are the phases of the two microwave electric fields in the first waveguide at the time the atom enters the guide. The phases ψ_1 and ψ_2 are the differences of the phases of the microwave electric fields in the first and second waveguides. To reflect the random arrival time of the atoms at the first waveguide, and the incoherence of frequencies ω_1 and ω_2, the calculated transition probability is subsequently averaged independently over δ_1 and δ_2. We will use the convention that ω_1 is the smaller of the microwave frequencies, the one fixed in phase and scanned in frequency; ω_2 is the larger, fixed frequency, which undergoes the relative phase change.

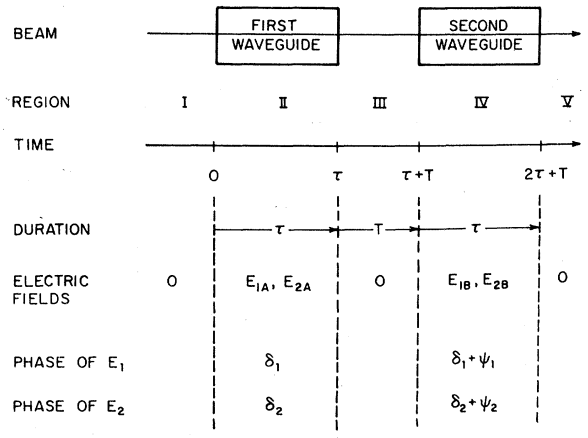

FIG. 3. A schematic view of the spectroscopy region showing the rf fields seen by an atom as it transverses the apparatus.

The interaction of hydrogen atoms with this electric field is assumed to be described by the Hamiltonian

$$\mathcal{H}=\mathcal{H}_0-q\vec{E}(t)\cdot\vec{r}\,, \quad (4)$$

where $q\vec{r}$ is the atomic electric-dipole-moment operator, and $\mathcal{H}_0$ the field-free atomic Hamiltonian. For the electric field specified above, only $\Delta m_F=0$ transitions occur, and dipole selection rules allow the coupling of incident $3\,^2S_{1/2}(F=0)$ states only to those $n=3$ states listed in Table I and shown in an energy-level diagram in Fig. 4. The table includes theoretically calculated energies of the states [relative to the $3\,^2S_{1/2}(F=0)$ state] including hyperfine energies, and also calculated decay rates. The diagonal entries of the Hamiltonian $\mathcal{H}_0$ are taken to be of the form

$$E_N=\omega_N-i\Gamma_N/2\,, \quad (5)$$

where ω_N is the Bohr frequency, and Γ_N the decay rate, of state N. The energy-level diagram gives the matrix elements of $\hat{z}$, in units of the Bohr radius, between the states coupled together by $\vec{r}$. As an abbreviation we will use S, P, P', D, and D' to designate, respectively, the $3\,^2S_{1/2}(F=0)$,

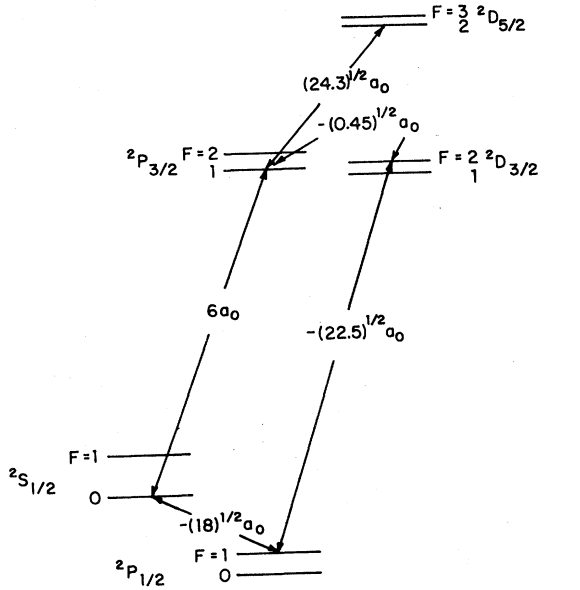

FIG. 4. Energy-level diagram (not to scale) for the $n=3$ manifold of atomic hydrogen depicting the electric-dipole transitions linked to the $3\,^2S_{1/2}(F=0)$ state by an electric field parallel to the z axis. The numbers beside the lines indicating linkage are the matrix elements of z; the unit a_0 is the Bohr radius.

TABLE I. Energy levels involved in the $^2S_{1/2}-{}^2D_{5/2}$ two-photon transition in the $n=3$ state of hydrogen. In the third column labeled energy, the location of the $3\,^2S_{1/2}$ state with the assumption there is no hyperfine splitting is taken as the origin, and none of the hyperfine splittings for the other states have been included. Column 4 gives the hyperfine energies that must be added to column 3 to obtain the energy levels when the hyperfine structure (hfs) is included. Column 5 gives the energy of the states when the hyperfine structure is included with the location of the $3\,^2S_{1/2}(F=0)$ state taken as the origin.

State	Mnemonic	Energy (MHz)	hfs (MHz)	ω (10^9 sec^{-1})	Γ (10^9 sec^{-1})
$3\,^2S_{1/2}(F=0)$	S	0.0	−39.457	0.0	0.0063
$3\,^2P_{3/2}(F=1)$	P	2935.191	−4.380	18.662 74	0.1897
$3\,^2P_{1/2}(F=1)$	P'	−314.898	+4.382	−1.703 11	0.1897
$3\,^2D_{5/2}(F=2)$	D	4013.197	−1.577	25.453 67	0.0647
$3\,^2D_{3/2}(F=2)$	D'	2929.859	+1.577	18.666 68	0.0647

$3\,^2P_{3/2}(F=1)$, $3\,^2P_{1/2}(F=1)$, $3\,^2D_{5/2}(F=2)$, and $3\,^2D_{3/2}(F=2)$ states. We are particularly interested in transitions from the $3\,^2S_{1/2}(F=0)$ state to the $3\,^2D_{5/2}(F=2)$ state via the $3\,^2P_{3/2}(F=1)$ state.

We want to calculate the amplitude

$$A(\omega_1,\omega_2,E_{1A},E_{1B},E_{2A},E_{2B},\psi_1,\psi_2,\delta_1,\delta_2) \tag{6}$$

for the transmission of an atom initially in the $3\,^2S_{1/2}(F=0)$ state through the two interaction regions. The experimentally observable transmission probability is given by

$$P(\omega_1,\omega_2,E_{1A},E_{1B},E_{2A},E_{2B},\psi_1,\psi_2)$$

$$=\left(\frac{1}{2\pi}\right)^2\int_0^{2\pi}d\delta_1\int_0^{2\pi}d\delta_2|A|^2\,. \tag{7}$$

The experimental signals are defined to be the fractional decrease of P upon application of the microwave power:

$$P_0=P(\omega_1,\omega_2,0,0,0,0,0°,0°)\,, \tag{8}$$

$$S(0°)=1-P(\omega_1,\omega_2,E_{1A},E_{1B},E_{2A},E_{2B},0°,0°)/P_0\,, \tag{9}$$

$$S(180°)=1-P(\omega_1,\omega_2,E_{1A},E_{1B},E_{2A},E_{2B},0°,180°)/P_0\,. \tag{10}$$

It is convenient to transform the 0° and 180° signals to "quenching" and "interference" signals, respectively:

$$Q=\tfrac{1}{2}[S(0°)+S(180°)]\,, \tag{11}$$

$$I=S(0°)-S(180°)\,. \tag{12}$$

The amplitude A can be expanded into five terms which correspond to the five ways in which an atom can propagate across the field-free region as follows:

$$\begin{aligned}A=&B_{SS}\exp(-iE_ST)A_{SS}\\&+B_{SP}\exp(-iE_PT)A_{PS}+B_{SP'}\exp(-iE_{P'}T)A_{P'S}\\&+B_{SD}\exp(-iE_DT)A_{DS}+B_{SD'}\exp(-iE_{D'}T)A_{D'S}\,.\end{aligned} \tag{13}$$

In this expression, A_{SS}, A_{PS}, $A_{P'S}$, A_{DS}, $A_{D'S}$ represent, respectively, the amplitudes for an atom to enter the first waveguide in the S state and emerge, respectively, the in S, P, P', D, D' states, and B_{SS}, B_{SP}, $B_{SP'}$, B_{SD}, $B_{SD'}$ represent the amplitudes for an atom to enter the second waveguide in, respectively, the S, P, P', D, D' states and emerge in the S state. Each of these ten amplitudes can be expanded in a double perturbation series in E_1 and E_2 of the form

$$A_{SS}=\sum_{n=0}^{\infty}A_{SS}^{(n)}\,, \tag{14}$$

where $A_{SS}^{(n)}$ is of nth order in the electric fields. Since the interaction Hamiltonian is a periodic function of δ_1 and δ_2, each of the amplitudes is a periodic function of δ_1 and δ_2 and can be further expanded into a double Fourier series:

$$A_{SS}=\sum_{n=0}^{\infty}\sum_{j,k=-n}^{n}A_{SS,jk}^{(n)}e^{ij\delta_1}e^{ik\delta_2}\,. \tag{15}$$

Similarly

$$B_{SS}=\sum_{n=0}^{\infty}\sum_{j,k=-n}^{n}B_{SS,jk}^{(n)}e^{ij\delta_1}e^{ik\delta_2}e^{ij\psi_1}e^{ik\psi_2}\,, \tag{16}$$

where the ψ_1, ψ_2 phase dependence has been shown explicitly. Time-dependent perturbation theory (TDPT) can be used to calculate each of the expansion coefficients.

Substitution into the expression for A gives the signal in terms of the calculable coefficients $A_{SS,jk}^{(n)}$, etc. After averaging over the phases δ_1 and δ_2, the following expression is obtained for the signal S:

$$S = -2\,\mathrm{Re}[e^{iE_S\tau}(A^{(2)}_{SS,00} + B^{(2)}_{SS,00})] - 2\,\mathrm{Re}[e^{iE_S\tau}(A^{(4)}_{SS,00} + B^{(4)}_{SS,00})] - \sum_{j,k=-2}^{2} |e^{iE_S\tau}|^2[\,|A^{(2)}_{SS,jk}|^2 + |B^{(2)}_{SS,jk}|^2]$$

$$-2\,\mathrm{Re}\left(\sum_{j,k=-2}^{2} e^{iE_S\tau}B^{(2)}_{SS,jk}e^{i(j\psi_1+k\psi_2)}[e^{iE_S\tau}(A^{(2)}_{SS,-j-k}) + e^{-iE_S\tau}(A^{(2)}_{SS,jk})^*]\right)$$

$$-2\,\mathrm{Re}\left(e^{(\Gamma_S-\Gamma_D)T/2}e^{\Gamma_S\tau}e^{i(\omega_S-\omega_D)T}e^{2i\omega_S\tau}\sum_{j,k=-2}^{2} B^{(2)}_{SD,jk}e^{i(j\psi_1+k\psi_2)}A^{(2)}_{DS,-j-k}\right)$$

$$+ O(E^6)$$

$$+ (\text{terms in } P,\ P',\ \text{and } D' \text{ states}). \tag{17}$$

The insertion of $\psi_1 = 0°$, $\psi_2 = 0°$ or 180°, corresponding to the experimentally achieved phase differences between the two interaction regions, gives $S(0°)$ and $S(180°)$ and in turn the I and Q signals. The most important terms for S in the interference signal are those involving the D state.

As an example of the TDPT technique, we write explicitly the form of the amplitude for $A^{(2)}_{DS,-1-1}$:

$$A^{(2)}_{DS,-1-1} = (2i\hbar)^{-2}\int_0^{\tau} dt_2 \int_0^{t_2} dt_1 e^{-iE_D(\tau-t_2)}\, e^{-i\omega_1 t_2}(qE_{1A}\langle D|z|P\rangle)\sin(\pi t_2/\tau)e^{-iE_P(t_2-t_1)}$$

$$\times e^{-i\omega_2 t_1}(qE_{2A}\langle P|z|S\rangle)\sin(\pi t_1/\tau)e^{-iE_S(t_1-0)} + (\text{term with } \omega_1 \text{ and } \omega_2 \text{ interchanged}). \tag{18}$$

This amplitude describes the absorption of one photon of frequency ω_1, and one of ω_2, in a transition from the S state at time $t = 0$ to the D state by time $t = \tau$. All the other 2nd- and 4th-order amplitudes can be evaluated in the same way; the integrations can be performed analytically, although the complexity of the results requires evaluation by computer. The expansion of the signal has been carried through to 6th order in electric fields, and the interference signal isolated; in this order the rf Stark shift, or power shift, of the two-photon resonance appears.

We have shown in Ref. 1, however, that these TDPT amplitudes can also be expressed using a much simpler effective-potential approximation. In this approximation, the 2nd-order amplitude $A^{(2)}_{DS,-1-1}$ is given by

$$A^{(2)}_{DS,-1-1} = (i\hbar)^{-1}\int_0^{\tau} dt e^{-iE_D(\tau-t)}V^A_{\mathrm{eff}}(D \leftarrow S)(t) \times e^{-iE_S(t-0)}, \tag{19}$$

where the effective potential is given by

$$V^A_{\mathrm{eff}}(D \leftarrow S)(t) = (4\hbar\alpha)^{-1}q^2E_{1A}E_{2A}\langle D|z|P\rangle\langle P|z|S\rangle \times \sin^2(\pi t/\tau)e^{-i(\omega_1+\omega_2)t}. \tag{20}$$

Here the quantity analogous to the energy defect is α, where

$$\alpha^{-1} = \left(\frac{E_S+E_D}{2} - E_P + \frac{\omega_1-\omega_2}{2}\right)^{-1} + \left(\frac{E_S+E_D}{2} - E_P - \frac{\omega_1-\omega_2}{2}\right)^{-1}. \tag{21}$$

In a similar manner, the methods of Ref. 1 can be used to calculate using TDPT the effective potentials for D to S, S to S, and D to D transitions. These effective potentials can then be used to calculate in a compact form all the amplitudes required for a determination of the signal through 6th order. The explicit expressions for the potentials with superscripts designating the waveguide to which they apply are

$$V^A_{\mathrm{eff}}(D \leftarrow S)(t) = \frac{q^2E_{1A}E_{2A}}{4\hbar\alpha}\langle D|z|P\rangle\langle P|z|S\rangle e^{-i(\omega_1+\omega_2)t}\sin^2(\pi t/\tau), \tag{22}$$

$$V^A_{\mathrm{eff}}(S \leftarrow D)(t) = \frac{q^2E_{1A}E_{2A}}{4\hbar\alpha}\langle S|z|P\rangle\langle P|z|D\rangle e^{i(\omega_1+\omega_2)t}\sin^2(\pi t/\tau), \tag{23}$$

$$V^B_{\mathrm{eff}}(D \leftarrow S)(t) = \frac{q^2E_{1B}E_{2B}}{4\hbar\alpha}\langle D|z|P\rangle\langle P|z|S\rangle e^{-i(\omega_1+\omega_2)t}e^{-i(\psi_1+\psi_2)}\sin^2[\pi(t-T-\tau)/\tau], \tag{24}$$

$$V^B_{\mathrm{eff}}(S \leftarrow D)(t) = \frac{q^2E_{1B}E_{2B}}{4\hbar\alpha}\langle S|z|P\rangle\langle P|z|D\rangle e^{i(\omega_1+\omega_2)}e^{i(\psi_1+\psi_2)}\sin^2[(t-T-\tau)/\tau], \tag{25}$$

$$V^A_{eff}(S\leftarrow S)=\sum_{N=P,P'}\sum_{j=1,2}\frac{q^2(E_{jA})^2}{4\hbar}\left(\frac{1}{E_S+\omega_j-E_N}+\frac{1}{E_S-\omega_j-E_N}\right)\langle S|z|N\rangle\langle N|z|S\rangle\sin^2(\pi t/\tau)\,, \tag{26}$$

$$V^B_{eff}(S\leftarrow S)=\sum_{N=P,P'}\sum_{j=1,2}\frac{q^2(E_{jB})^2}{4\hbar}\left(\frac{1}{E_S+\omega_j-E_N}+\frac{1}{E_S-\omega_j-E_N}\right)\langle S|z|N\rangle\langle N|z|S\rangle\sin^2[\pi(t-T-\tau)/\tau]\,, \tag{27}$$

$$V^A_{eff}(D\leftarrow D)(t)=\sum_{j=1,2}\frac{q^2(E_{jA})^2}{4\hbar}\left(\frac{1}{E_D+\omega_j-E_P}+\frac{1}{E_D-\omega_j-E_P}\right)\langle D|z|P\rangle\langle P|z|D\rangle\sin^2(\pi t/\tau)\,, \tag{28}$$

$$V^B_{eff}(D\leftarrow D)(t)=\sum_{j=1,2}\frac{q^2(E_{jB})^2}{4\hbar}\left(\frac{1}{E_D+\omega_j-E_P}+\frac{1}{E_D-\omega_j-E_P}\right)\langle D|z|P\rangle\langle P|z|D\rangle\sin^2(\pi(t-T-\tau)/\tau]\,. \tag{29}$$

For the calculation of the interference signal in lowest order (E^4), the important terms are $A^{(2)}_{DS,-1-1}$ and $B^{(2)}_{SD,11}$. The use of the effective potentials gives

$$A^{(2)}_{DS,-1-1}=(i\hbar)^{-1}\int_0^\tau dt e^{-iE_D(\tau-t)}V^A_{eff}(D\leftarrow S)e^{-iE_S(t-0)}$$

$$=\frac{q^2E_{1A}E_{2A}}{2\hbar^2\alpha}\langle D|z|P\rangle\langle P|z|S\rangle\left(\frac{\pi}{\tau}\right)^2\frac{e^{i\beta\tau}-1}{\beta[\beta^2-(2\pi/\tau)^2]}e^{-iE_D\tau}\,, \tag{30}$$

where

$$\beta=E_D-E_S-(\omega_1+\omega_2) \tag{31}$$

is the complex detuning factor. In a similar manner

$$B^{(2)}_{SD,11}=\frac{q^2E_{1B}E_{2B}}{2\hbar^2\alpha}\langle S|z|P\rangle\langle P|z|D\rangle\left(\frac{\pi}{\tau}\right)^2\frac{e^{-i\beta\tau}-1}{\beta[\beta^2-(2\pi/\tau)^2]}e^{-iE_S\tau}\,. \tag{32}$$

Together with the simplifying assumption that the two waveguides are equivalent so that

$$E_{1A}=E_{1B}=E_1\,, \tag{33a}$$

$$E_{2A}=E_{2B}=E_2\,, \tag{33b}$$

these amplitudes give to fourth order for the interference signal

$$I=2\left(\frac{q^2E_1E_2}{4\hbar^2}\right)^2|\langle S|z|P\rangle|^2|\langle P|z|D\rangle|^2$$

$$\times\left(\frac{2\pi}{\tau}\right)^4\mathrm{Re}\left(\frac{1}{\alpha^2}\frac{\sin^2(\beta\tau/2)}{\beta^2[\beta^2-(2\pi/\tau)^2]^2}e^{-i\beta(T+\tau)}\right). \tag{34}$$

Comparison of the interference signal calculated using the effective-potential approximation with the results of the fourth-order TDPT results mentioned earlier shows that the interference line shapes calculated with the two methods have line centers which agree to better than 1 kHz out of linewidths and center frequencies of roughly 10 and 4000 MHz, respectively.

To understand Eq. (34) it is instructive to make simplifying assumptions. First, assume that the decay of the states can be ignored so that α and β are real. The interference-signal line shape is then given by

$$1\propto\frac{1}{\alpha^2}\left(\frac{2\sin(\beta\tau/2)}{\beta[\beta^2-(2\pi/\tau)^2]}\right)^2\cos\beta(T+\tau)\,. \tag{35}$$

This form shows the factorization into cosine "interference wiggles" whose width is determined by $T+\tau$, the transit time between the centers of the two interaction regions, and an envelope function which is independent of T. The distance between the zero crossings of the interference signal as ω_1 is varied is

$$\Delta\omega_1=\frac{3.14}{T+\tau}\,. \tag{36}$$

The FWHM of the envelope is

$$\Delta\omega_1=\frac{9.05}{\tau}\,. \tag{37}$$

The quenching envelope is considerably wider than the interference signal even when $T\rightarrow 0$.

The inclusion of the atomic decay rates, by treating α and β as complex, has several effects. First, the width of the quenching envelope is increased from the transit-time-limited value. Second, the period of the interference wiggles is increased corresponding to the increased importance of the late regions of the first, and early regions of the second, interacting region due to the decay of the atomic states. The effective interaction time, $T+\tau$, for the interference wiggles is changed to $T+\tau-k$, where

$$k=\tau\left(\coth x-\frac{1}{x}\frac{\pi^2+3x^2}{\pi^2+x^2}\right), \tag{38}$$

and

$$x=\frac{(\Gamma_D-\Gamma_S)\tau}{4}. \tag{39}$$

For the measurement reported in this paper, the uncorrected interaction time $T+\tau$ (the time of flight between the center of the two waveguides) was roughly 80 nsec, and the correction was 4 nsec. Third, the lifetime-induced phase of the energy defect causes a shift of the center and some asymmetry in the interference signal analogous to the lifetime shift discussed earlier. The inclusion of this shift gives for the center of the interference signal

$$\omega_1+\omega_2=\omega_D-\omega_S-\frac{2\psi}{T+\tau-k}, \tag{40}$$

where ψ is the phase of α^{-1} which is given by

$$\alpha^{-1}=|\alpha|^{-1}e^{i\psi}. \tag{41}$$

In practice this corresponds to a shift of the interference signal by 0.83% of the distance between zero crossings.

In addition to this lifetime shift, which persists even in the limit of zero electric fields, there are "power shifts" which result from the effective-potential terms coupling S to S and D to D, specifically $V^A_{eff}(S\rightarrow S)(t)$, $V^A_{eff}(D\rightarrow D)(t)$, $V^B_{eff}(S\rightarrow S)(t)$, and $V^B_{eff}(D\rightarrow D)(t)$. These terms are not included in the interference line shape calculation to order E^4, but are important in the order-E^6 calculation, where the power shifts first appear. In sixth order the center of the line shape varies linearly with E_1^2 and E_2^2; the resonant frequency increases as E_1^2 or E_2^2 increases. In addition there is an additional asymmetry introduced into the line shape for the interference signal; the general character of the line shape is not significantly different from the fourth-order calculation. In principle, the calculations may be extended to any order in E; the calculations, however, become very unwieldly for the higher orders.

A more efficient method for calculating the line shape to higher order is to use the effective-potential terms in a 2×2 Hamiltonian which describes the time evolution of only the S and D states, and not that of the P, P', and D' states. The 2×2 Hamiltonian is

$$\mathcal{H}^N_{eff}=\begin{pmatrix}E_S & 0\\ 0 & E_D\end{pmatrix}+\begin{pmatrix}V^N_{eff}(S\leftarrow S)(t) & V^N_{eff}(S\leftarrow D)(t)\\ V^N_{eff}(D\leftarrow S)(t) & V^N_{eff}(D\leftarrow D)(t)\end{pmatrix}, \tag{42}$$

where $N=A,B$ correspond to the two waveguides, and

$$\mathcal{H}_{eff}=\begin{pmatrix}E_S & 0\\ 0 & E_D\end{pmatrix} \tag{43}$$

for $\tau<t<\tau+T$.

The effect of the on-diagonal effective-potential terms, $V^N_{eff}(S\leftarrow S)(t)$ and $V^N_{eff}(D\leftarrow D)(t)$, is to shift the energies of the S and D states, respectively, while the off-diagonal terms induce transitions between the S and D states. By performing an appropriate time average of the on-diagonal terms, one finds an expression for the linear power shift

$$\Delta\omega_1=\mathrm{Re}\left[\tfrac{1}{2}(\Lambda_D-\Lambda_S)\left(\frac{\tau-k'}{T+\tau-k}\right)\right], \tag{44}$$

where

$$k'=k+\frac{3\chi\tau}{\chi^2+4\pi^2}, \tag{45}$$

$$\Lambda_D=\sum_{j=1,2}\frac{q^2(E_j)^2}{4\hbar}\langle D|z|P\rangle\langle P|z|D\rangle\left(\frac{1}{E_D+\omega_j-E_P}+\frac{1}{E_D-\omega_j-E_P}\right), \tag{46}$$

$$\Lambda_S=\sum_{N=P,P'}\sum_{j=1,2}\frac{q^2(E_j)^2}{4\hbar}\langle S|z|N\rangle\langle N|z|S\rangle\left(\frac{1}{E_S+\omega_j-E_N}+\frac{1}{E_S-\omega_j-E_N}\right). \tag{47}$$

The factor of $\frac{1}{2}$ arises from averaging over the sinusoidal shape of the electric fields, and the factor of $(\tau-k')/(T+\tau-k)$ gives the dilution of the power shift of the interference signal corresponding to the fraction of the time that atoms spend in the intermediate, field-free region. The k and k' are small corrections to the times due to the finite lifetimes of the S and D states. Since Λ_S and Λ_D are second order in the electric fields, in this approximation the power shifts are linear in microwave power for each microwave frequency.

A simple numerical integration of Schrödinger's equation using the 2×2 Hamiltonian (Eq. 42) produces line shapes relevant to the actual experimental conditions. Since the assumptions used for the derivation of the effective potential terms do not depend significantly upon the strength of the electric fields (Ref. 1), this approach is capable of describing correctly the resonance line shape even under conditions of power saturation, as was demonstrated for the single-field experiment.[2] Simulated line shapes using this approach were generated for all of the experimental data and used in the data reduction to account for the line-shape asymmetry. The power shift deduced from the

simulations agrees with Eq. (44) to better than 1% accuracy, and is linear in E_1^2 and E_2^2. Deviation from linearity could also arise from a nonlinear dependence of Λ_S and Λ_D on power. Higher-order approximations of the effective-potential terms used to calculate Λ_S and Λ_D exclude this possibility. Thus, for the purposes of data reduction, it can be assumed that the power shift is bilinear in E_1^2 and E_2^2.

Finally we briefly mention other features of the line shape which are not yet included in the line shape theory. The only effect of importance is the "$\vec{v}\times\vec{B}$" shift, a line shift resulting from the additional component of the electric field which arises from the Lorentz transformation of the longitudinal microwave magnetic fields present in the waveguides used in the experimental interaction region. The largest shifts in the interference resonances due to this mechanism were calculated using TDPT to be less than 0.4% of the linewidth. The other nonidealities in the experimental apparatus, such as holes in the side walls of the waveguides, stray polarizations of electric fields, microwave magnetic fields, and dc magnetic and electric fields, are all too small to shift the interference lines by more than 0.1% of their linewidths.

IV. APPARATUS

Figure 5 shows a schematic drawing of the apparatus. The setup was a modification of that used in the measurements with a single microwave interaction region.[2]

A fast beam of hydrogen atoms was produced by charge exchange from a H^+ or H_3^+ beam. The data reported in this paper were obtained using either a 42-keV H^+ beam or a 78-keV H_3^+ beam. The microwave interaction region consisted of two parallel waveguides with the longitudinal axis of propagation perpendicular to the atomic-beam axis. The microwaves in the guides propagated in the TE_{10} mode, and the electric field was perpendicular to the beam axis. The internal width of the waveguides was 12.94 cm, and the two adjacent inner walls of the two waveguides were separated by a 7.11-cm field-free region.

The state-selection region described in the earlier paper[2] was located immediately following the second waveguide. An applied 330-MHz radio-frequency electric field was used to quench atoms in the $3\,^2S_{1/2}(F=1)$ state and preferentially transmit atoms in the $3\,^2S_{1/2}(F=0)$ state.

Surviving atoms in the $3\,^2S_{1/2}(F=0)$ state were detected by observing the Balmer-α photons (656 nm) emitted when they decayed to the $2\,^2P_{1/2,3/2}$ states. An active quencher, in which a microwave field mixed through a two-photon transition the $3\,^2S_{1/2}$ and $3\,^2D_{5/2}$ states, was used to shorten the effective lifetime of atoms in the $3\,^2S_{1/2}$ state and thus increase the probability for decay in front of the phototube. The simpler $3\,^2S_{1/2}-3\,^2P_{1/2,3/2}$ mixing was not used because the atoms in the $3\,^2P_{1/2,3/2}$ state decay 89% of the time to the $1\,^2S_{1/2}$ state with the emission of Lyman-β photons, and we did not have an efficient Lyman-β detector. The microwave mixing was performed using a resonant cavity at a frequency of 2027 MHz with electric fields of about 25 V/cm. In addition to increasing the signal by a factor of 3, this quenching scheme also increased the hyperfine selectivity, since atoms in the $3\,^2S_{1/2}(F=1)$ state would require roughly 2002 MHz for resonant two-photon quenching. A 656-nm, 10-nm bandwidth interference filter, and a C31034 photomultiplier tube were used to observe the Balmer-α photons.

The last element in the beam line was a Faraday cup. The Faraday cup was used to measure the instantaneous current of the unneutralized fraction of the beam (about 50%). This measurement of the instantaneous current was employed to correct the observed photon count rates for short-term variations in the rate of production of atoms in the $3\,^2S_{1/2}(F=0)$ state.

Figure 6 shows a schematic diagram of the microwave system used to observe the resonances. The objective is to produce in the waveguides microwave fields with frequencies ν_1 and ν_2 such that $\psi_1=0°$, $E_{1A}=E_{1B}$ independent of the variable frequency ν_1, and $\psi_2=0°$ or 180°, $E_{2A}=E_{2B}$ for the fixed frequency ν_2.

The microwave fields with frequencies ν_1 and ν_2 were derived, respectively, from a programmable synthesizer and a locked klystron oscillator. The

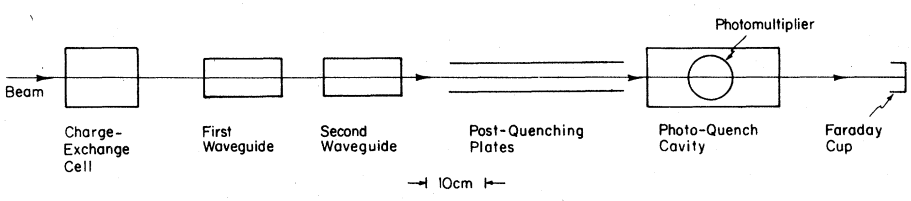

FIG. 5. Schematic diagram of the apparatus.

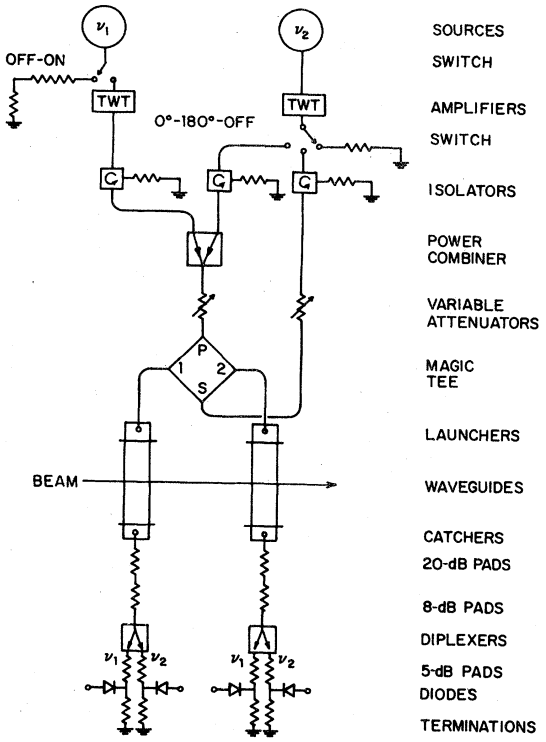

FIG. 6. Schematic diagram of the microwave system used to observe the resonances.

former was tuneable from 1 to 2000 MHz; the latter was locked at 2155.000 MHz. The high power levels required to drive the two-photon transitions were obtained by using broadband traveling-wave tube (TWT) amplifiers with a nominal 30-dB gain and 20-W output in both the ν_1 and ν_2 channels. Low-pass filters following the TWT amplifiers ensured the rejection of harmonics.

Fast diode switches were used to control the flow of microwave power. A low-power switch proceeding the TWTA was employed to turn off and on the ν_1 channel. A single-pole, three-throw high-power switch following the ν_2 TWT amplifier was used to switch the ν_2 channel between the off, $\psi_2 = 0°$, and $\psi_2 = 180°$ configurations. Both switches had more than 60-dB isolation in the off position.

A coaxial "magic tee" was used to obtain the phase and power division required to drive the two waveguides. The power at frequency ν_1 was always delivered to the P port of the tee; this resulted in equal power appearing in phase at the output ports. The power at frequency ν_2 was switched alternatively between the P and S ports of the tee; this resulted in equal powers appearing, respectively, in or 180° out of phase at the output ports. Since the tee is a passive linear device obeying the superposition principle, these divisions were obtained when power at both frequencies ν_1 and ν_2 was present in the tee. The accuracy of the power and phase division of the tee was roughly 2 parts in 10^3; this corresponds to greater than 56-dB S to P port isolation. The data were taken in such a manner as to cancel effects due to the residual phase errors. A narrow-band, low-loss power combiner incorporating two 90° hybrid tees and a variable-length trombone line was used to combine the powers at frequencies ν_1 and ν_2 at the P port of the tee.

The power at the output ports of the tee was conducted to the waveguides by matched semirigid coaxial cables, and launched into the waveguides by coaxial (TEM_{00}) to waveguide (TE_{10}) transformers. After propagating through the waveguides, the power was caught and reconverted to coaxial propagation by identical transformers. The power was then attentuated by successive 20 and 8-dB attenuators attached to each "catcher" and applied to the power-monitoring system.

The power-monitoring system made possible independent monitoring for superposed ν_1 and ν_2 powers through the use of diplexers following each 8-dB attenuator. These passive linear devices consisted of high- and low-pass filters, each with a 2-GHz rollover frequency, tied to a common input port. Their isolation against "crosstalk" in the outputs is >60 dB for frequencies >100 MHz away from the 2-GHz crossover frequency. The result is a nearly perfect separation of the incident superposed powers into separate ν_1 and ν_2 channels. On the output of each waveguide, the microwave power at each of the two frequencies was detected with a microwave diode. For each frequency the voltages from the two diodes were summed and measured with voltage-to-frequency converters (VFC).

V. DATA-TAKING PROCEDURE

Data were taken in a three-phase switching arrangement with a sequencer controlling the microwave switches in such a manner as to obtain a preset number of 64-msec counting cycles. Each cycle consisted of four 16-msec counting periods with the sequence microwave power off, microwave power on with $\psi_2 = 0$, microwave power off, microwave power on with $\psi_2 = 180°$. The outputs of the photomultiplier tube counting Balmer-α photons and the VFC's monitoring the beam intensity and microwave power were synchronously gated into a bank of counters so that data for the off, 0°, and 180° counting periods were separately accumulated. After a preset number of counting cycles, the data were read into a Data General minicomputer, processed, and stored. The mi-

crowave frequencies and powers were set and adjusted manually between data points; generally three 64-sec counting intervals were combined and constituted one datum.

The counter totals were processed as follows. First the photon count rate was corrected for the dark-current rate of the photomultiplier tube and the voltage-to-frequency-converter counts monitoring the beam were corrected for the rate with no beam. The number of photons per unit beam was obtained by dividing the corrected photon count rate by the corresponding corrected beam counts. The 0° signal [$S(0°)$] was then calculated from the expression

$$S(0°)=\frac{\Phi_{off}-\Phi_{(0°)}}{\Phi_{off}}, \tag{48}$$

where Φ represents the number of photons per beam and the subscript, the rf signal state. A similar expression was used to calculate $S(180°)$. The "interference" and "average quenching" signals, I and Q, were calculated using Eqs. (11) and (12).

The statistical errors deduced from the mutual consistency of nominally identical data points were consistent with the errors expected from photon counting statistics and were generally on the order of 0.1%. The magnitude of the I and Q signals depended on the beam speed and microwave power levels; they were, respectively, 0.3 to 1.6% and 3 to 7%.

Data were taken with hydrogen atoms derived from a 78-keV H_3^+ beam and 42-keV H^+ beam. At each energy line scans were made to study the overall line shape and to determine the correction due to the overlap of the undesired hyperfine components. Figure 7 shows line scans for both the quenching and interference signals plotted as a function of $(\nu_1+\nu_2)$ obtained in preliminary studies with a 53-keV H^+ beam and no hyperfine quenching. Figures 8 and 9 show the quenching signals for hydrogen atoms derived from the 42-keV H^+ beam and the 78-keV H_3^+ beam as a function of ν_1 with ν_2 fixed at 2155.000 MHz. The desired $3\,^2S_{1/2}(F=0)-3\,^2D_{5/2}(F=2)$ resonance occurs near $\nu_1=1897$ MHz; the resonances originating in the $3\,^2S_{1/2}(F=1)$ state lie near $\nu_1=1848$ MHz. The data for Fig. 8 were obtained with only the photo-Q hyperfine selection field; the data for Fig. 9 were obtained with both the photo-Q and post-Q hyperfine selection fields. Data such as those shown in Fig. 9 were used to determine the amplitude of the residual components of the $F=1$ hyperfine transitions for use in correcting the interference data. Figure 10 shows a line scan for the interference curve obtained with the 78-keV H_3^+ beam and only the photo-Q hyperfine selection field.

The method of symmetric points was used to take data for the determination of the fine-structure interval. Figure 11 shows the pattern in

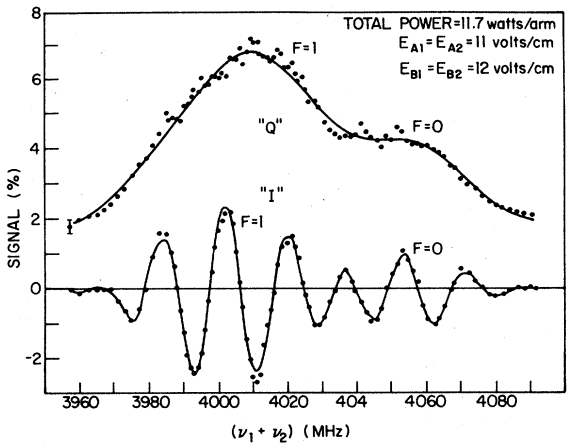

FIG. 7. Line scans for the quenching and interference signals plotted as a function of $(\nu_1+\nu_2)$. These data were obtained in preliminary studies with hydrogen atoms derived from a 53-keV H^+ beam and no hyperfine quenching.

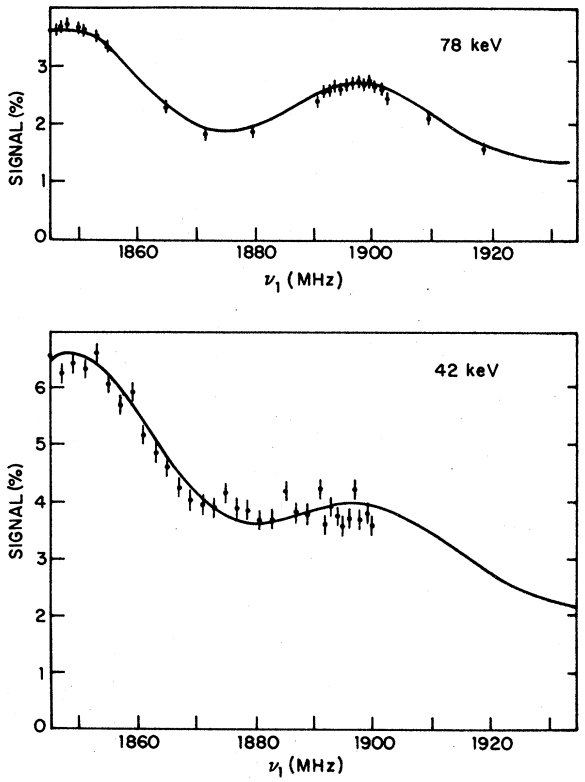

FIG. 8. Line scans obtained for the quenching signal with a 42-keV H^+ beam and a 78-keV H_3^+ beam. The photo-Q hyperfine selecting field was on and the post-Q hyperfine selecting field was off.

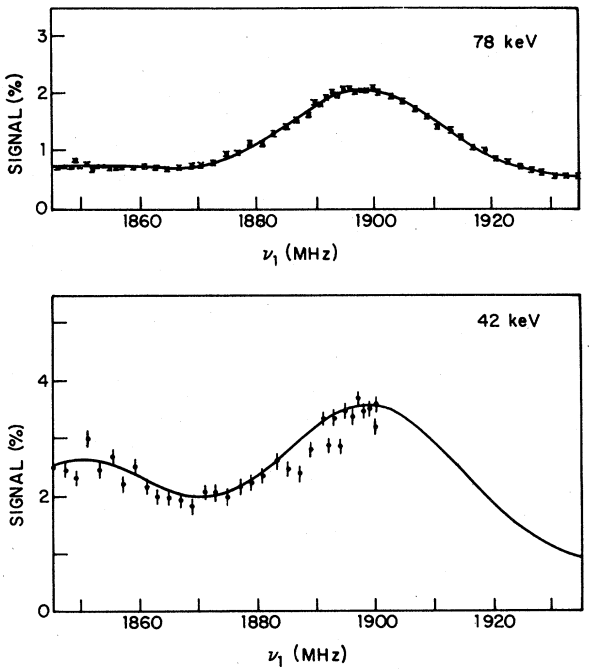

FIG. 9. Line scans obtained for the quenching signal with a 42-keV H^+ beam and a 78-keV H_3^+ beam. Both the photo-Q and post-Q hyperfine selecting fields were on.

which the data were taken. Three 64-sec measurements were made at each frequency, and the three results were combined to determine the average and the standard deviation of the average. For each configuration the interference signal was measured at 11 frequencies. Eight of the frequencies gave four independent measurements of the line center based on symmetric point spacings of 3, 6, 9, and 18 MHz for the 78-keV H_3^+ data and 4, 8, 12 and 24 MHz for the 42-keV H^+ data. The remaining three frequencies were chosen to be the central maximum and the neighboring minima of the interference curve. A group of 12 measurements at the 11 frequencies constituted one run. Each run was repeated under nominally identical conditions with the time order in which the points were taken mirror reversed about the line center

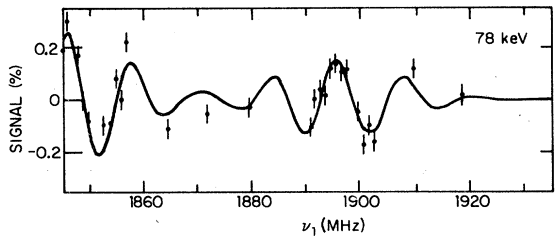

FIG. 10. A line scan for the interference signal obtained with a 78-keV H_3^+ beam and only the photo-Q hyperfine selecting field[illegible]

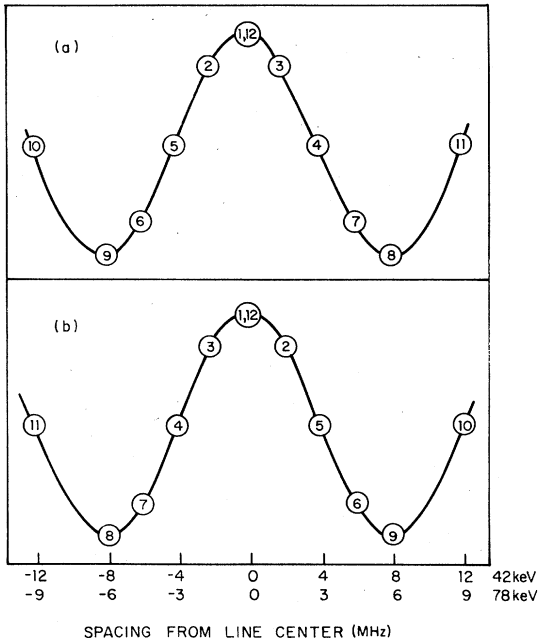

FIG. 11. A diagram showing the manner in which the symmetric-points data were taken. For each configuration a run was made with the order shown in part (a) and a run was made with the order shown in part (b). The numbers at the bottom of the figure indicate the frequency scale for, respectively, hydrogen atoms derived from the 42-keV H^+ beam and the 78-keV H_3^+ beam.

as shown in Fig. 11. Each pair of such runs was made with each of four combinations of voltages of the power-monitoring diodes corresponding to low and high values of E_1^2 and E_2^2. Such a set of 8 runs was taken in each of the 8 configurations obtained by interchanging the ports of the magic tee used to drive the two waveguides, by reversing the direction in which the microwaves propagated in the waveguides, and by interchanging the two waveguides together with their driving and power-monitoring systems. Figure 12 shows the first four of these configurations. These interchanges were used to cancel frequency shifts due to phase errors in the rf system and the first-order Doppler shift. In all, 64 runs were made at each of the two beam energies.

The microwave-power-monitoring system was used to determine the microwave electric field in the waveguides. The calibration technique used was similar to that employed earlier and involved calibration of the diodes using a power meter, calibration of the diplexers and attenuators, measurement of the reflection coefficients of the "catchers," and use of the theoretical formula relating the transmitted power and microwave voltage level in a waveguide. The calibration program also provides a measurement of the degree to which the

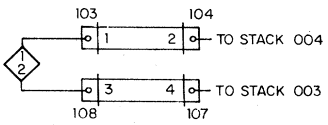

ARRANGEMENT	TEE PORT	LAUNCHER	WAVEGUIDE	CATCHER	STACK
A	1	103	1-2	104	004
	2	108	3-4	107	003
B	2	103	1-2	104	004
	1	108	3-4	107	003
C	2	104	2-1	103	004
	1	107	4-3	108	003
D	1	104	2-1	103	004
	2	107	4-3	108	003

DESCRIPTION OF STACKS

STACK	ATTENUATORS		DIPLEXER	DIODES	
	20 dB	8 dB		ν_1	ν_2
003	1	6769	003	101	A
004	2	6772	004	102	2

FIG. 12. A description of the arrangement of the microwave apparatus used for each of the configurations A, B, C, and D. The drawing at the top depicts case A.

actual microwave electric fields approached the ideal behavior assumed in the theoretical analysis (Eq. 33). We found worst-case imbalances in the electric fields in the two waveguides up to 12% (e.g., $E_{2B} = 1.12\,E_{2A}$) produced chiefly by different reflection coefficients of the catchers on the two waveguides. Simulations using the numerical methods described earlier showed that the shifts due to such imbalances were less than 1 kHz. The measurements showed that the values of E_2 differed at most by 0.2% when the microwave system was driven in the 0° and 180° states. This would produce shifts less than 4 kHz. The measurements of E_1 as a function of ν_1 showed that $dE_1/d\nu_1$ was less than 0.02%/MHz; this would produce at most a shift of 5 kHz. Table II summarizes the summed diode voltages and the microwave fields for the various power levels at which data were taken. We estimate the errors to be assigned to these values of electric field squared are 3.8%, compounded from an observed scatter of 1.6% in microwave calibration measurements, 1.9% in absolute calibration of the power meter, 2.0% for systematic errors in the measurement of catcher reflection coefficients, and 2.0% for second-order effects of multiple reflections within the waveguides. For the symmetric-points data the summed diode voltages were 0.2000 and 0.3000 V for E_1 and 0.3200 and 0.4800 V for E_2. For the line-scan data the voltages were 0.2500 and 0.4000 V for E_1 and E_2, respectively. Any deviations from these nominal values were accounted for by making small corrections to the measured signals. These power corrections were very small and generally about one-tenth the statistical error of a datum.

TABLE II. A summary of the average microwave electric fields squared at frequencies ν_1 and ν_2 for each of the diode sum voltages and microwave configurations used to take line-scan and symmetric-points data.

Sum voltage V_1 (V)	Values of E_1^2 Microwave arrangement (V^2/cm^2) A	B	C	D
0.2000	116.4	117.2	119.8	119.3
0.2500	144.6	145.6	148.2	147.7
0.3000	172.8	173.8	177.1	176.6
	Values of E_2^2			
0.3200	87.8	87.9	80.0	80.1
0.4000	116.4	116.4	106.1	106.0
0.4800	146.4	146.4	133.5	133.4

VI. DATA AND RESULTS

Figure 13 shows typical symmetric-points data taken at 42 and 78 keV with, respectively, the H^+ and H_3^+ beams. In this section we shall describe how such data were used to determine the $3\,^3S_{1/2} - 3\,^2D_{5/2}$ fine-structure interval.

As a first step in the data reduction, we fit to each of the 128 runs a simple cosine curve, with the amplitude, center frequency, and period as adjustable parameters. Figure 13 shows two examples of such fits. From the measured period, the known width and separation of the waveguides, and the theory for the width of the interference signal, we found for the atomic velocities

$$V_{42} = 0.296(3)\ \text{cm/nsec},$$

$$V_{78} = 0.227(2)\ \text{cm/nsec},$$

for the H(3S) atoms derived, respectively, from the 42-keV H^+ and the 78-keV H_3^+ beams. The calculated speeds were consistent from run to run and agreed with, but were more precise than, speeds deduced from the masses of the ions and the measured accelerator voltages.

The measured symmetric-point signals and the slopes (i.e., variations in signal with respect to frequency) deduced from the cosine fits were then used to compute the symmetric-points centers for each of the pairs of symmetric points. We will

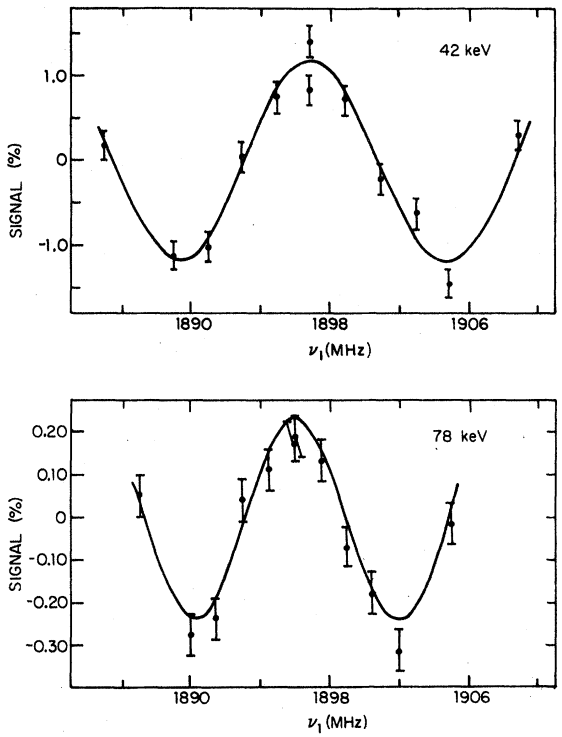

FIG. 13. Plots showing typical symmetric-points data taken at 42 and 78 keV with, respectively, the H^+ and H_3^+ beams.

use the mnemonics H, M, L, and O for the symmetric-point pairs located high, middle, low, and outside on the interference line shape, corresponding to frequency separations of 3, 6, 9, and 18 MHz in the 78-keV data and 4, 8, 12, and 24 MHz in the 42-keV data.

The 512 symmetric-point centers thus obtained from the 128 runs were further condensed to 32 averages, by averaging over the four instrumental interchanges discussed previously. Comparison of centers obtained in successive, nominally identical runs revealed variations consistent with the assigned errors. Results obtained with different magic-tee orientations were averaged to cancel out the phase-division errors; results obtained with different directions of microwave propagation were averaged to cancel first-order Doppler shifts; results obtained with opposite time order of the waveguides were averaged to cancel phase errors arising from different electrical lengths of the two waveguide structures. The 32 average centers resulting from this procedure are listed in Table III.

The data were compared with the symmetric-points centers calculated theoretically using the procedure described earlier. For these calculations the $[3^2S_{1/2}(F=0)-3^2D_{5/2}(F=2)]$ fine-structure separation was assumed to be 4051.077 MHz, and ν_2 was assumed to be 2155.000 MHz. The second-order Doppler shift was calculated using the measured velocity and included in the simulation. The calculated value for ν_1 was expressed in the form

$$\nu_1=\nu_0+\delta\nu_{2D}+\alpha E_1^2+\beta E_2^2\,, \tag{49}$$

where

$$\nu_0=(4051.077-2155.000)+\Delta\nu \tag{50a}$$

$$=1896.077+\Delta\nu\,. \tag{50b}$$

Here $\Delta\nu$ is the correction to the position of the symmetric-points-determined center due to the lifetime shift and the $\vec{v}\times\vec{B}$ effect, $\delta\nu_{2D}$ is the second-order Doppler shift, and α and β are coefficients giving the dependence of the line center on the magnitudes of the microwave electric fields.

TABLE III. A summary of average symmetric-point centers obtained by combining the data obtained with different time order, with reversal of the magic tee, with reversed direction of propagation for the microwaves, and with interchange of the two waveguides.

Power		42-keV centers Symmetric-point center (MHz)			
E_1^2	E_2^2	H	M	L	O
low	low	1896.511(162)	96.307(118)	96.548(203)	96.438(140)
high	low	96.673(119)	96.609(85)	96.613(126)	96.533(87)
low	high	96.701(118)	96.652(83)	96.492(128)	96.775(85)
high	high	96.802(87)	96.828(66)	96.798(106)	96.727(69)
			78-keV centers		
low	low	1895.953(233)	95.964(161)	96.385(225)	96.284(163)
high	low	96.168(169)	96.006(118)	96.350(173)	96.200(122)
low	high	96.140(160)	96.221(110)	96.304(150)	96.358(111)
high	high	96.648(114)	96.573(79)	96.260(116)	96.347(81)

TABLE IV. A summary of the calculated position and the dependence of the calculated position of the centers of the symmetric-point pairs on the amplitude of the two-microwave electric fields. The predicted frequency is given by the expression $\nu_1 = \delta\nu_{2D} + \nu_0 + \alpha E_1^2 + \beta E_2^2$, where $\nu_0 = 1896.077 + \Delta\nu$.

Symmetric point spacing (MHz)	Mnemonic	$\delta\nu_{2D}$ (MHz)	$\Delta\nu$ (MHz)	ν_0 (MHz)	α (MHz cm^2/V^2)	β (MHz cm^2/V^2)
				42-keV H^+		
4	H	−0.198	−0.061	1896.016	0.002 73	0.004 72
8	M	−0.198	−0.056	96.021	0.002 63	0.004 54
12	L	−0.198	−0.038	96.039	0.002 29	0.003 96
24	O	−0.198	−0.052	96.025	0.002 60	0.004 50
				78-keV H_3^+		
3	H	−0.116	−0.047	1896.030	0.002 79	0.004 83
6	M	−0.116	−0.045	96.032	0.002 67	0.004 63
9	L	−0.116	−0.037	96.040	0.002 28	0.003 94
18	O	−0.116	−0.045	96.032	0.002 55	0.004 43

These results together with the measured values of the microwave electric field strengths summarized in Table II were used to calculate the predicted symmetric-points centers which are directly comparable to the experimental entries in Table III. The results of these calculations are summarized in Table IV. Table V summarizes the differences between the experimental and theoretical values of the various symmetric-points centers. If the assumed value for the S-D fine-structure interval and the assigned absolute microwave powers were correct, then all the residuals would be statistically consistent with zero. The average residual for the 42-keV data is −0.092(25) with a χ^2 of 8.7 for 15 degrees of freedom; the average residual for the 78-keV data is −0.546(31) with a χ^2 of 20.6 for 15 degrees of freedom.

To test further for a systematic dependence of the residuals on microwave power or the symmetric-points spacing, the residuals for each beam speed and symmetric-points spacing were fit to the expression

$$\delta\nu = \delta\nu_0 + (\delta\alpha)E_1^2 + (\delta\beta)E_2^2 .$$

The fit quantities $\delta\alpha$ and $\delta\beta$, which would be zero for perfect consistency of the data with theory, give a measure of any discrepancy between the observed and predicted power shifts. Similarly $\delta\nu_0$ is a measure of the discrepancy between the

TABLE V. The difference between the experimental and calculated positions of the symmetric-point pairs for the several combinations of microwave electric fields.

Power E_1^2	Power E_2^2	H	M	L	O	Av	χ^2
			42-keV residuals Symmetric-point pairs (MHz)				
low	low	−0.041(162)	−0.221(118)	+0.108(203)	−0.062(140)	−0.097(74)	2.3
high	low	−0.038(119)	−0.071(85)	+0.042(126)	−0.113(87)	−0.061(50)	1.1
low	high	−0.122(118)	−0.136(83)	−0.170(128)	+0.027(85)	−0.084(49)	2.7
high	high	−0.120(87)	−0.112(66)	+0.006(106)	−0.167(69)	−0.115(39)	1.9
	Av	−0.092(56)	−0.121(42)	−0.019(66)	−0.089(54)		
	χ^2	0.5	1.1	2.1	3.2		
			78-keV residuals				
low	low	−0.680(233)	−0.644(161)	−0.142(255)	−0.316(163)	−0.456(93)	5.0
high	low	−0.620(169)	−0.751(118)	−0.307(173)	−0.549(122)	−0.592(69)	4.7
low	high	−0.758(160)	−0.641(110)	−0.444(150)	−0.494(111)	−0.576(63)	3.0
high	high	−0.404(114)	−0.439(79)	−0.619(116)	−0.653(81)	−0.532(47)	5.5
	Av	−0.561(77)	−0.572(54)	−0.554(92)	−0.557(55)		
	χ^2	3.8	5.8	0.9	3.9		

observed and the predicted zero-power line center. The results of these fits are summarized in Table VI.

For both beam speeds the average values of $\delta\alpha$ and $\delta\beta$ are consistent with zero. This indicates that the average power shift is that predicted by the theory. For the 42-keV H^+ data the four individual values of $\delta\alpha$ and $\delta\beta$ are consistent with 0 with χ^2 values of 3.9 and 0.8, respectively, for three degrees of freedom. For the 78-keV H_3^+ data the four individual values of $\delta\alpha$ and $\delta\beta$ scatter badly about their mean with, respectively, χ^2 values of 7.2 and 8.4 for three degrees of freedom.

The same pattern of behavior is shown by the results for $\delta\nu_0$. The average values for the two beam speeds agree with the previously obtained mean residual, with somewhat larger errors. The consistency of the individual results for $\delta\nu_0$ with their mean is good for the 42-keV H^+ data with $\chi^2 = 2.1$ for 3 degrees of freedom. The consistency of the individual results for $\delta\nu_0$ for the 78-keV results is bad with a χ^2 of 14.9 for 3 degrees of freedom.

From this statistical analysis we concluded that the 42-keV data are internally consistent, but that the 78-keV data are not internally consistent. The 78-keV data behave reasonably when averaged over all four symmetric-point spacings but are internally inconsistent when examined more closely. The "H" and "M" symmetric points show power shifts much larger than expected; the "L" and "O" points show power shifts much smaller than expected. The reason for this misbehavior is not known. It is clear, however, that the 78-keV data must be regarded with suspicion. Rather than expanding the error bars in the 78-keV data so as to cover over the internal inconsistency, we have chosen not to include the 78-keV data in the determination of the fine-structure interval.

TABLE VI. The results of the fits of the residuals to the expression $\delta\nu = \delta\nu_0 + (\delta\alpha)E_1^2 + (\delta\beta)E_2^2$.

	$\delta\nu_0$	$\delta\alpha$	$\delta\beta$
42-keV H^+	(MHz)	(MHz cm^2/V^2)	
H	+0.077(415)	0.000 04(208)	−0.001 46(212)
M	−0.313(305)	0.001 19(150)	0.000 07(154)
L	−0.039(503)	0.001 70(240)	−0.002 03(243)
O	+0.324(337)	−0.002 64(159)	−0.000 16(164)
Av	−0.004(185)	−0.000 17(90)	−0.000 59(92)
χ^2	2.1	3.9	0.8
78-keV H_3^+			
H	−1.524(575)	0.004 58(284)	+0.002 05(295)
M	−1.308(396)	0.001 84(195)	0.003 67(205)
L	+0.683(564)	−0.003 02(276)	−0.005 52(295)
O	+0.225(405)	−0.003 20(200)	−0.002 33(209)
Av	−0.506(232)	−0.000 19(114)	−0.000 08(120)
χ^2	14.9	7.2	8.4

Table VII summarizes the corrections and the estimated uncertainties for the 42-keV H^+ data. The statistical error was determined from the data in the manner described earlier. The lifetime and $(\vec{v}\times\vec{B})$-shift uncertainties are estimates based on an analysis of the line-shape theory used to determine these corrections. The entry for the power-shift uncertainty represents 3.8% of the average power-shift correction, corresponding to the error assigned to the absolute power scale. The second-order Doppler-shift error was determined from the error in the beam speed. The hyperfine-overlap error comes from an estimate of the uncertainty in the hyperfine composition of the observed line and the sensitivity of the theoretical line shape to variations in the hyperfine-overlap parameters.

The next two errors arise from estimates of imperfections in the microwave system. The first, for phase repeatability, is assigned on the basis of observed variations in the shift of the line center caused by the reversal of the magic tee, and corresponds physically to variations in the electrical lengths of the microwave connections to the waveguide upon disassembly and reassembly. The second error, for a false interference signal, corresponds to a measured (1σ) limit on the slope of the "interference" signal determined in a geometry with the waveguides spaced so widely that there is no true S-D interference signal. The observed signals proved to be consistent with zero

TABLE VII. A summary of the corrections and estimated errors for the determination of the $^2S_{1/2}(F=0) - {}^2D_{5/2}(F=2)$ fine-structure interval from the 42-keV H^+ data. All frequencies are in MHz.

Correction (MHz)	
Simulation input	4051.077
Mean residual	−0.092
Hyperfine overlap	+0.001
Net interval	4050.986
Uncertainties (MHz)	
Statistical	0.025
Lifetime shift	0.005
$\vec{v}\times\vec{B}$ shift	0.010
Microwave power scale	0.025
Second-order Doppler shift	0.004
Hyperfine overlap	0.012
Phase repeatability	0.031
False interference signal	0.025
Quadratic power shift	0.010
Stark and Zeeman effect	0.005
Net error	0.057

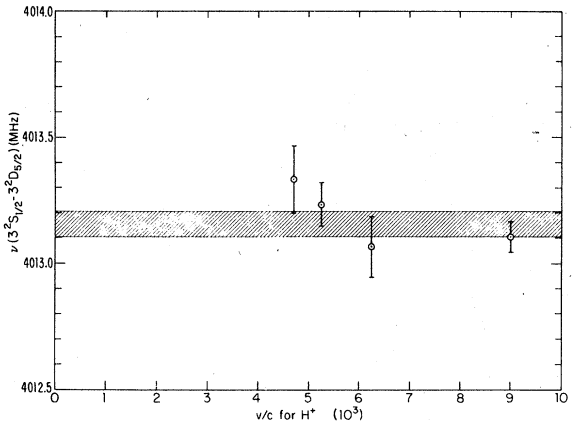

FIG. 14. A plot showing the several measured values of the $3^2S_{1/2}-3^2D_{5/2}$ fine-structure interval as a function of the velocity of the hydrogen atoms on which the measurements were made.

value and zero slope, within errors. Physically this corresponds to a measurement of power imbalance between the 0° and 180° parts of the microwave switching cycle, which would produce quenching signals whose difference would be an "interference" signal unrelated to real S-D interference.

The final two entries in the error budget arise from estimates of the joint effect of true quadratic power shifts in the theoretical line center and of nonlinearities in the microwave power scale, and of the effects of dc Stark and Zeeman effects on the line center. The net uncertainty was determined by adding in quadrature the several components. The final measured value for the $3^2S_{1/2}$ $(F=0)-3^2D_{5/2}(F=2)$ fine-structure interval is

$$\nu[3^2S_{1/2}(F=0)-3^2D_{5/2}(F=2)]=4050.986(57)\ \text{MHz}.$$

Combining this value with the calculated hyperfine-structure intervals for the $3^2S_{1/2}$ and $3^2D_{5/2}$ states, we obtain for the $3^2S_{1/2}-3^2D_{5/2}$ fine-structure interval

$$\nu(3^2S_{1/2}-3^2D_{5/2})=4013.106(57)\ \text{MHz}.$$

VII. CONCLUSIONS

In the single-field measurement reported earlier, the value obtained for the $3^2S_{1/2}-3^2D_{5/2}$ fine-structure interval was

$$\nu(3^2S_{1/2}-3^2D_{5/2})=4013.204(89)\ \text{MHz}.$$

This value agrees satisfactorily with the value obtained in this measurement. Figure 14 shows in graphic form the three independent values obtained in the earlier measurement and the result for the 42-keV H^+ data reported in this paper (see Table VIII) as a function of the velocity of the beam. Combining the two measurements, we obtain as a final value for the $3^2S_{1/2}-3^2D_{5/2}$ fine-structure interval

$$\nu(3^2S_{1/2}-3^2D_{5/2})=4013.155(53)\ \text{MHz}.$$

This value agrees satisfactorily with the prediction of quantum electrodynamics

$$\nu(3^2S_{1/2}-3^2D_{5/2})=4013.197(7)\ \text{MHz}.$$

The results of this measurement are somewhat disappointing in their final precision, and we do not feel that they demonstrate the full potential of the technique. The major limitation in the precision was due to a poor signal in the final configuration. There was a large background which was not completely understood, and the signal was not as large as anticipated.

The internal inconsistency of the 78-keV H_3^+ data was disconcerting, and several attempts were made to understand it as indicative of systematic shifts due to unknown effects. One hypothesis was that hydrogen atoms produced by collision-induced breakup of H_3^+ carry with them a molecu-

TABLE VIII. Independent fast-beam measurements of the $3^2S_{1/2}-3^2D_{5/2}$ fine-structure interval.

Source	Beam	Fields	Result (MHz)	$10^3\,v\,[H(3s)]/c$
Ref. 1	28-keV H_3^+	single	4013.316(138)	4.70
Ref. 1	36-keV H_3^+	single	4013.232(100)	5.25
Ref. 1	53-keV H_3^+	single	4013.064(126)	6.25
This work	42-keV H^+	separated	4013.106(57)	9.87

lar-ion partner which shifts the fine structure. The agreement of the results with an H^+ beam and the earlier single-radio-frequency measurements with an H_3^+ beam do not support this suggested explanation unless the effect is strongly dependent on beam velocity.

ACKNOWLEDGMENTS

This research was supported by the NSF under Grants No. PHY 76-14857 and PHY 78-09657. One of the authors (D.A.V.B.) acknowledges support of the Charles Bayne Aiken Foundation.

---

*Present address: Joint Institute for Laboratory Astrophysics, University of Colorado, Boulder, Colo. 80309.

†Present address: Schlumberger-Doll Research Center, Ridgefield, Conn. 06877.

[1]D. A. Van Baak, B. O. Clark, and F. M. Pipkin, Phys. Rev. A 19, 787 (1979).

[2]B. O. Clark, D. A. Van Baak, S. R. Lundeen, and F. M. Pipkin, Phys. Rev. A 19, 802 (1979).

[3]C. W. Fabjan and F. M. Pipkin, Phys. Rev. A 6, 556 (1972).

[4]S. R. Lundeen and F. M. Pipkin, Phys. Rev. Lett. 34, 1368 (1975).

[5]P. B. Kramer, S. R. Lundeen, B. O. Clark, and F. M. Pipkin, Phys. Rev. Lett. 32, 635 (1974).

[6]B. O. Clark, D. A. Van Baak, and F. M. Pipkin, Phys. Lett. A 62, 78 (1977).